24th Applied Aerodynamics Conference
5 - 8 June 2006, San Francisco, California

AIAA 2006-3847

Kinetic-Eddy Simulation of Static and Dynamic Stall

Yichuan Fang[#] and Suresh Menon[*]
School of Aerospace Engineering
Georgia Institute of Technology, Atlanta, GA 30332

Abstract

A Kinetic-Eddy Simulation (KES) approach has been developed for large-eddy simulation (LES) of wall-bounded turbulent flow at high Reynolds numbers. The model solves for the local unresolved kinetic energy and the local subgrid length scale. The dissipation of the kinetic energy depends on the length scale, as well as on the length scale gradient. In most of flow domain of simulated cases, the subgrid length scale is of the order of the computational grid scale, and the KES approach behaves like a LES. In some other regions the length scale tends toward the integral scale and thus, smoothly approaches the very large-eddy simulation (VLES) limit. A robust KES approach is demonstrated here that employs the realizability constraints to bound the model parameters. The realizable KES has been applied to static stall around a 3D NACA0015 wing, oscillatory attached and dynamic light stall, and dynamic deep stall flows around a 2D NACA0015 airfoil. Vortex shedding and massive separation of the boundary layer at high Reynolds number are clearly captured. The behavior of the realizable KES approach on high angle-of-attack aerodynamics is studied.

I. Introduction

Dynamic stall is an important phenomenon in rotorcraft aerodynamics and is the result of airfoils/wings pitching with a maximum angle of attack (AoA) greater than the static-stall angle. It has challenged aerodynamicists for many years to accurately understand the physics behind dynamic stall. There have been many numerical simulations of this problem. However past predictions using RANS model are not satisfactory and may introduce some uncertainties in the prediction of rotorcraft aerodynamics (Sankar, *et al*., 2002). It is well understood that the dynamic effects are more closely associated with the detachment and the reattachment of turbulent vortices on the pitching airfoils/wings, and the subsequent vortex motion in the wake region. The phenomenon is characterized by a massive separation at high Reynolds number and by the formation of large-scale vortical structures. As a result, the maximum values of lift, drag, and pitching moment highly exceed their static values.

The flow around airfoils/wings at large angles of attack is complicated. It includes adverse pressure gradient, streamline curvature, boundary layer separation, and transition from laminar to turbulent flow. There is also a singularity at the flow stagnation point around the airfoil leading edge (LE). The flow is sensitive to the airfoil geometry, angle of attack, and Reynolds number. Because of the strong coupling between the trailing edge (TE) separation and the pressure peak at the leading edge, all the regions around the airfoil are equally important. However, few existing models have the capability to model all the flow regions with equal accuracy.

[#] Postdoctoral Fellow, senior Member AIAA
[*] Professor, AIAA Associate Fellow

The massively separated flow associated with dynamic stall is highly unsteady away from the wall. The Reynolds-Averaged Navier-Stokes (RANS) approaches, which are designed to solve the steady state, time-averaged flows, are not expected to predict this kind of turbulent flow well. Direct numerical simulation (DNS) would of course be the ideal method, if computational resource is available. Large-Eddy Simulaiton (LES) is the current choice, which is an intermediate technique between DNS and RANS. In LES, the contribution of the large, energy-containing structures and all scales larger than the grid resolution to momentum and energy transfer is computed exactly, and only the effect of unresolved small scales is modeled. Similar to DNS, LES maintains spatial and temporal accuracy of the resolved scales. However, LES is still extremely expensive, requiring fairly fine meshes especially in the near-wall region. In a wall-resolved LES, the distance from the wall to the first grid should be at least less than two wall units ($y_1^+ < 2$), in order to resolve the instantaneous velocity gradient close to the wall and capture the near wall structures sufficiently (Piomelli and Chasnov, 1996). Thus, it is apparent that even a pure LES is nearly beyond current computer capacity for resolving wall turbulence at high Reynolds numbers. As a tradeoff in between, a class of hybrid RANS-LES methods has been proposed to alleviate the LES near-wall resolution requirement. In the hybrid methods, a RANS model is employed in the near-wall region, and LES closure is used away from it. Among them, detached eddy simulation (DES) (Spalart *et al*., 1997; Squires, 2004) and other zonal approaches (Martin, *et al*., 2006) have shown some impressive results for complex aerodynamic applications. But there is usually an explicit specification of a distance to the wall or a blending function to couple the RANS and LES method, which may introduce significant grid dependency into the simulation. Partially averaged Navier-Stokes (PANS) method, based on k-ε (Girimaji and Abdol-Hamid, 2005) or k-ω (Lakshmipathy and Girimaji, 2006), has been recently proposed as a hybrid method and the results are encouraging.

Kinetic-Eddy Simulation (KES) approach (Fang and Menon, 2006) has been recently proposed for LES simulation of high Reynolds number turbulent flows. KES is a two-equation subgrid model, which solves for the subgrid kinetic energy and the subgrid length scales locally. In principle, KES becomes very large-eddy simulation (VLES) when only large scales of turbulence are resolved with very coarse grid; LES when scales close to grid scale are resolved; and direct numerical simulation (DNS) in the limit of very fine grid, i.e., the subgrid length scale and subgrid kinetic energy tend to vanish. KES is applicable to near-wall turbulence without any ad-hoc distance from the wall specification or viscous damping. This model has been applied, in the past, to 2D flows around a NACA-0015 airfoil at various AoAs, with good agreement with experimental measurement.

In this study, the KES approach is more generalized for 3D flows and made more robust by applying the realizability constraints (Schumann, 1977; Vremann, *et al.*, 1994) on the subgrid closure. KES with realizability constraint is used here to simulate 3D static stall around a NACA0015 wing and dynamic stall around a NACA0015 airfoil. The numerical results have been compared with available experimental, and good agreement is observed. In Section 2, the KES subgrid model will be presented briefly. The application of the realizability constraint is discussed in Section 3. The numerical implementation of the model is described in Section 4, and the KES results are given in Section 5. We conclude and discuss future work in Section 6.

II. KES Subgrid Model

The detailed development of KES model has been described in a previous work (Fang and Menon, 2006). In this section, KES model will be briefly introduced to establish the methodology developed in this work for completeness.

Filtered Navier-Stokes Equations

The equations governing the motion of the resolved eddies can be obtained by separating the large scales from the small scales. LES equations are obtained using a Favre (density-weighted) spatial filtering of the unsteady, compressible Navier-Stokes equations. A filtered variable is defined as $\widetilde{f} = \overline{\rho f} / \overline{\rho}$. Applying the filtering operation, the resolved transport equations of mass, momentum, and energy can be obtained in a conservative form as

$$\frac{\partial \overline{\rho}}{\partial t} + \frac{\partial}{\partial x_i}\left(\overline{\rho}\widetilde{u}_i\right) = 0\,, \tag{1}$$

$$\frac{\partial \overline{\rho}\widetilde{u}_j}{\partial t} + \frac{\partial}{\partial x_i}\left[\overline{\rho}\widetilde{u}_i\widetilde{u}_j + \overline{p}\delta_{ij} - \widetilde{\tau}_{ij} + \tau_{ij}^{\,sgs}\right] = 0\,, \tag{2}$$

$$\frac{\partial \overline{\rho}\widetilde{E}}{\partial t} + \frac{\partial}{\partial x_i}\left[(\overline{\rho}\widetilde{E} + \overline{p})\widetilde{u}_i - \widetilde{\tau}_{ij}\widetilde{u}_j + \widetilde{q}_i + E_i^{\,sgs} + p_i^{\,sgs} + \sigma_i^{\,sgs} + q_i^{\,sgs}\right] = 0\,, \tag{3}$$

where ρ is the density, u_i is the velocity in the x_i direction, p is the pressure, and E ($= e + \frac{1}{2}u_i^{\,2}$) is the total energy per unit mass. The filtered total energy is defined as $\widetilde{E} = \widetilde{e} + \frac{1}{2}\widetilde{u}_i^{\,2} + k^{sgs}$, which includes the subgrid kinetic energy $k^{sgs} = \frac{1}{2}(\overleftrightarrow{u_i u_i} - \widetilde{u}_i\widetilde{u}_i)$. Here, the overhead symbol "$\leftrightarrow$" represents the Favre filtering. The resolved molecular viscous stress and heat fluxes are given by $\widetilde{\tau}_{ij} = -2\overline{\mu}\left(\widetilde{S}_{ij} - \frac{1}{3}\widetilde{S}_{kk}\delta_{ij}\right)$, $\widetilde{q}_i = -\overline{\kappa}\,\partial\widetilde{T}/\partial x_i$, where $\widetilde{S}_{ij} = \frac{1}{2}(\partial\widetilde{u}_i/\partial x_j + \partial\widetilde{u}_j/\partial x_i)$ is the strain-rate tensor. $\overline{\mu}$ and $\overline{\kappa}$ are the molecular viscosity and the thermal conductivity at the filtered temperature $\widetilde{T}$, respectively. The subgrid terms that require closure are:

$$\tau_{ij}^{\,sgs} = \overline{\rho}(\overleftrightarrow{u_i u_j} - \widetilde{u}_i\widetilde{u}_j)\,, \tag{4}$$

$$E_i^{\,sgs} = \overline{\rho}(\overleftrightarrow{E\,u_i} - \widetilde{E}\,\widetilde{u}_i)\,, \tag{5}$$

$$P_i^{\,sgs} = \overline{p\,u_i} - \overline{p}\,\widetilde{u}_i\,, \tag{6}$$

$$\sigma_i^{\,sgs} = \overleftrightarrow{\tau_{ij}u_j} - \widetilde{\tau}_{ij}\widetilde{u}_j\,, \tag{7}$$

$$q_i^{sgs} = \overline{\kappa\frac{\partial T}{\partial x_i}} - \overline{\kappa}\frac{\partial\widetilde{T}}{\partial x_i}\,. \tag{8}$$

Subgrid Shear Closure

The subgrid stress tensor $\tau_{ij}^{\,sgs}$ is modeled using an eddy viscosity model (EVM) as,

$$\tau_{ij}^{\,sgs} = -2\overline{\rho}\nu_t[\widetilde{S}_{ij} - \frac{1}{3}\widetilde{S}_{kk}\delta_{ij}] + \frac{2}{3}\overline{\rho}k^{sgs}\delta_{ij} \tag{9}$$

where the subgrid eddy viscosity ν_t is proportional to the product of the subgrid velocity scale, $\sqrt{k^{sgs}}$, and the subgrid length scale, l^{sgs} , defined as,

$$\nu_t = C_\nu\sqrt{k^{sgs}}\,l^{sgs} \tag{10}$$

In the KES approach, k^{sgs} and l^{sgs} are obtained by solving the following k^{sgs} - and $(kl)^{sgs}$ - transport equations:

$$\frac{\partial\overline{\rho}k^{sgs}}{\partial t} + \frac{\partial\overline{\rho}\widetilde{u}_i k^{sgs}}{\partial x_i} = \tau_{ij}^{\,sgs}\frac{\partial\widetilde{u}_i}{\partial x_j} - C_{\varepsilon,k}\overline{\rho}\frac{(k^{sgs})^{3/2}}{l^{sgs}} + \frac{\partial}{\partial x_i}\left(\overline{\rho}(\frac{\nu}{\mathbf{Pr}} + \frac{\nu_t}{\sigma_k})\frac{\partial k^{sgs}}{\partial x_i}\right), \tag{11}$$

$$\frac{\partial\overline{\rho}(kl)^{sgs}}{\partial t} + \frac{\partial\overline{\rho}\widetilde{u}_i(kl)^{sgs}}{\partial x_i} = C_l l^{sgs}\tau_{ij}^{\,sgs}\frac{\partial\widetilde{u}_i}{\partial x_j} - C_{\varepsilon,kl}\overline{\rho}(k^{sgs})^{3/2} + \frac{\partial}{\partial x_i}\left(\overline{\rho}(\frac{\nu}{\mathbf{Pr}} + \frac{\nu_t}{\sigma_{kl}})\frac{\partial(kl)^{sgs}}{\partial x_i}\right). \tag{12}$$

Here, the dissipation coefficient of $(kl)^{sgs}$ is a function of subgrid length gradient given as (Fang and Menon, 2006)

$$C_{\varepsilon,kl} = 0.58 + 2\frac{C_\nu}{\sigma_k}\left(\frac{\partial l^{sgs}}{\partial x_j}\right)^2 . \qquad (13)$$

The coefficient **Pr** is laminar Prandtl number, taken to be 0.72. The dissipation coefficient of subgrid k^{sgs} is $C_{\varepsilon,k} = 0.916$, and the Prandtl-Schmidt number for subgrid k^{sgs} is $\sigma_k = 0.9$. $C_\nu = 0.0667$ is the eddy viscosity coefficient. The same coefficients, $C_{\varepsilon,k}$, σ_k and C_ν , were employed in k-equation LES simulations by Chakravarthy and Menon (2001). The production coefficient of subgrid $(kl)^{sgs}$ is $C_l = 1.06$, which has been obtained by combining the production of turbulent energy and the production of turbulent energy dissipation. The Prandtl-Schmidt number for subgrid $(kl)^{sgs}$ $\sigma_{kl} = 2$. The coefficients, C_ν and $C_{\varepsilon,k}$, can be obtained as a part of the solution by using a local dynamic kinetic model (LDKM), as shown in earlier literatures (Kim and Menon, 1999; Nelson and Menon,1997), which is in progress and will be reported in the future.

Here, the length scale, l^{sgs} , is a natural scale to bridge LES with DNS and VLES. Theoretically, when the length scale, l^{sgs} , is close to the computational grid size Δ , it approaches LES; when the computational grid size Δ becomes as small as the Kolmogrov length scale η, the subgrid length scale l^{sgs} should vanish in the limit of DNS; when the length scale, l^{sgs} , becomes much larger than Δ , then it approaches the integral length scale and KES becomes very large-eddy simulation (VLES). These limiting features still need to be proven further and full evaluation of the KES approach is planned in the near future to properly validate and establish this methodology. Also note that since l^{sgs} is a continuous function, there will be regions where this model will predict neither LES nor VLES. The performance of KES in this intermediate region is of particular interest in this study.

Subgrid Energy Transport Closure

In addition to the closure for τ_{ij}^{sgs} of equation (7), there are other unclosed terms appearing the LES filtered energy equation. In this work, SGS heat conduction q_i^{sgs} is ignored, and SGS total energy E_i^{sgs} , SGS pressure diffusion P_i^{sgs} , and SGS viscous work σ_i^{sgs} are explicitly closed as,

$$E_i^{sgs} = -\frac{\overline{\rho}\nu_t}{\sigma_e}\frac{\partial \widetilde{E}}{\partial x_i}, \qquad (14)$$

$$P_i^{sgs} = -\frac{\overline{\rho}\nu_t}{\sigma_p}\frac{\partial \overline{P}}{\partial x_i}, \qquad (15)$$

$$\sigma_i^{sgs} = -\tau_{ij}^{sgs}\widetilde{u}_j, \qquad (16)$$

where σ_e and σ_p are the effective subgrid Prandtl-Schmidt numbers for energy and pressure, respectively. At present they are taken as σ_k (=0.9).

III. Realizability Constraints

As mentioned above, the turbulent stresses are not computed explicitly in the eddy viscosity model (EVM) of KES. Eddy viscosity is calculated from the turbulent kinetic energy, k^{sgs} , and length scale, l^{sgs} . If they are not controlled in the EVM calculation, negative values of k^{sgs} and l^{sgs} may occur resulting in numerical instability. By setting proper limiters on k^{sgs} and l^{sgs} , negative values can be avoided without changing the flow solutions. These limiters can be obtained from the realizability constraints.

The realizability constraints of LES (Vremann, *et al.*, 1994; Nelson and Menon, 1998) are

$$\tau_{\alpha\alpha}^{sgs} \geq 0\,, \tag{17a}$$

$$\left(\tau_{\alpha\beta}^{sgs}\right)^2 \leq \tau_{\alpha\alpha}^{sgs}\tau_{\beta\beta}^{sgs} \quad \text{for } \alpha \neq \beta\,, \tag{17b}$$

$$\mathbf{det}\left(\tau_{\alpha\beta}^{sgs}\right) \geq 0\,, \tag{17c}$$

where the summation convention is not applied to the subscript index α and β, with $\alpha = 1, 2, 3$ and $\beta = 1, 2, 3$. Equation (17a) requires that the trace of the model SGS shear is nonnegative and equation (17b) states that the cross-correlation between the velocity components is bounded by the magnitude of autocorrelations.

Equation (17a) implies that

$$\tau_{11}^{sgs} + \tau_{22}^{sgs} + \tau_{33}^{sgs} \geq 0\,. \tag{18}$$

When equation (9) is substituted into this equation, $\overline{\rho} k^{sgs} \geq 0$. Considering that the filtered density is always positive, it can be concluded that

$$k^{sgs} \geq 0 \tag{19}$$

Equation (17b) implies that

$$\left(\tau_{12}^{sgs}\right)^2 + \left(\tau_{13}^{sgs}\right)^2 + \left(\tau_{23}^{sgs}\right)^2 \leq \tau_{11}^{sgs}\tau_{22}^{sgs} + \tau_{11}^{sgs}\tau_{33}^{sgs} + \tau_{22}^{sgs}\tau_{33}^{sgs} \tag{20}$$

Substituting equation (9) into this equation gives

$$\begin{aligned}\left(2\nu_t\right)^2\left(\widetilde{S}_{12}^2 + \widetilde{S}_{13}^2 + \widetilde{S}_{23}^2\right) \leq \left(2\nu_t\right)^2\left(\widetilde{S}_{11}\widetilde{S}_{22} + \widetilde{S}_{11}\widetilde{S}_{33} + \widetilde{S}_{22}\widetilde{S}_{33}\right) + 3\left(\nu_t \tfrac{2}{3}\widetilde{S}_{kk} + \tfrac{2}{3}k^{sgs}\right)^2 \\ - \left(\nu_t \tfrac{2}{3}\widetilde{S}_{kk} + \tfrac{2}{3}k^{sgs}\right)\left(2\nu_t\right)\left(2\widetilde{S}_{11} + 2\widetilde{S}_{22} + 2\widetilde{S}_{33}\right)\end{aligned} \tag{21}$$

Note that here $\widetilde{S}_{kk} = \widetilde{S}_{11} + \widetilde{S}_{22} + \widetilde{S}_{33}$. Equation (21) can be simplified as

$$\nu_t^{\,2}\left(\widetilde{S}_{12}^2 + \widetilde{S}_{13}^2 + \widetilde{S}_{23}^2\right) \leq \nu_t^{\,2}\left(\widetilde{S}_{11}\widetilde{S}_{22} + \widetilde{S}_{11}\widetilde{S}_{33} + \widetilde{S}_{22}\widetilde{S}_{33}\right) + \frac{1}{3}\left(k^{sgs\,2} - \nu_t^{\,2}\widetilde{S}_{kk}^{\,2}\right) \tag{22}$$

The terms inside the first set of parentheses in the right-hand-side of equation (22) can be rewritten as,

$$\widetilde{S}_{11}\widetilde{S}_{22} + \widetilde{S}_{11}\widetilde{S}_{33} + \widetilde{S}_{22}\widetilde{S}_{33} = \frac{1}{2}\widetilde{S}_{kk}^2 - \frac{1}{2}\left(\widetilde{S}_{11}^2 + \widetilde{S}_{22}^2 + \widetilde{S}_{33}^2\right) \tag{23}$$

Substituting equation (23) into equation (22) finally fields,

$$k^{sgs} \geq \frac{\sqrt{3}}{C_\alpha}\nu_t\sqrt{2\widetilde{S}_{ij}\widetilde{S}_{ji} - \frac{2}{3}\widetilde{S}_{kk}^2} \tag{24}$$

Here the operation of summation convention is applied to the subscript indices, $\widetilde{S}_{ij}\widetilde{S}_{ji}$ is the magnitude square of the mean strain rate. In the derivation, an assumption of positive filter (top-hat and Gaussian) is employed, and the eddy viscosity ν_t is always positive. This equality presents another lower bound for the turbulent kinetic energy k^{sgs}. It can be seen that equation (24) implies equation (19), and the realizability constraints of equation (17b) is stricter than equation (17a). Equation (17c) is equal to equation (17b) in a two dimensional problem. But the constraint of equation (17c) is generally stricter than equation (17b) in three dimensions, which gives a bigger value of the lower bound for k^{sgs} in equation (24). The analytical analysis of equation (17c) is much more difficult. In this work the constraint coefficient is taken $C_\alpha = 1$. The lower bound for k^{sgs} provides realizable information on the isotropic part of the turbulent stress in equation (9). This is of particular interest in a compressible kinetic-eddy simulation.

Substituting equation (9) into equation (24) yields,

$$C_\nu = \mathbf{min}(C_\nu, C_{\nu,\mathbf{lim}}) \tag{25}$$

where

$$C_{\nu,\mathbf{lim}} = \frac{1}{\sqrt{6}s}, \text{ with } s = \frac{l^{sgs}}{\sqrt{k^{sgs}}}\sqrt{\widetilde{S}_{ij}\widetilde{S}_{ji} - \frac{1}{3}\widetilde{S}_{kk}^2}$$

Here s is a dimensionless strain invariant, which represents the ratio of subgrid turbulent time scale, $t^{sgs} = l^{sgs}/\sqrt{k^{sgs}}$, to a characteristic resolved shear time scale, $\widetilde{t} = \left(\widetilde{S}_{ij}\widetilde{S}_{ji} - \frac{1}{3}\widetilde{S}_{kk}^2\right)^{-0.5}$. Equation (25) adjusts the eddy viscosity and kinetic energy production based on this ratio of turbulent time scale when the turbulent time scale, t^{sgs}, is over-predicted in flow region where strong velocity gradients exist. Equation (25) is used in equations (11-12). Similarly, Durbin (1996) proposed a similar limiter for incompressible flow to suppress the overproduced production in the region near a stagnation point, known as the *stagnation point anomaly*. The equation (24) should be applied to $(kl)^{sgs}$-equation (12) to set constraint on l^{sgs} also. Substituting equation (9) into equation (24) also gives,

$$l^{sgs} = \mathbf{min}(l^{sgs}, l^{sgs}_{\mathbf{lim}}) \tag{26}$$

where

$$l^{sgs}_{\mathbf{lim}} = \frac{1}{\sqrt{6}}\frac{\sqrt{k^{sgs}}}{C_\nu}\left(\widetilde{S}_{ij}\widetilde{S}_{ji} - \frac{1}{3}\widetilde{S}_{kk}^2\right)^{-0.5}$$

As will be shown in the results, the limiters of equations (25-26) make the KES approach more generalized and more robust in simulations of high Reynolds number turbulent flows.

IV. Numerical Approach

The LES filtered equations along with the KES subgrid model equations (11-12) are integrated by a dual time-stepping procedure (Jameson, 1991) and discretized by the finite volume method (FVM) in this work. A second-order accurate, three-point backward differencing is used in the physical time discretization, and the modified five-stage Runge-Kutta scheme (Jameson, *et al*., 1981; Jameson, 1991) is implemented for the pseudo-time evolution of solutions between the physical time steps. A cell-centered second-order scheme is applied in the space discretization. In order to eliminate spurious fluctuations, the second- and fourth-order Jameson artificial dissipations (Jameson, 1991), based on pressure gradient, are applied. The viscous coefficients of 1/4 and 1/256 are employed for the second- and fourth-order dissipation.

The far-field characteristic boundary condition (Jameson, 1985) is specified at the outer boundary of the C-grid by computing one dimensional Riemann invariants. At the outflow boundary, zero gradient condition is generally applied for the flow variables. On the wall, conditions of no-slip velocity and adiabatic wall temperature are used, zero normal-gradient of pressure and density are employed with the first-order extrapolation. On a moving wall, a normal gradient condition is applied to pressure as follows,

$$\frac{\partial p}{\partial n} = -\rho \boldsymbol{n}\cdot\boldsymbol{a}, \tag{27}$$

where $\boldsymbol{n}$ is the unit vector of wall in normal direction, and $\boldsymbol{a}$ the velocity acceleration vector of moving wall. Periodic boundary conditions are applied in the spanwise direction.

Both of k^{sgs} and l^{sgs} are set to zero on the wall. Wall function conditions can be avoided if computational grid solution is very fine ($y_1^+ < 1$) near the wall. Based on the analyses of energy dissipation rate on the wall, the following values are imposed on the first cells above the surface,

$$k^{sgs} = 0.25\nu\left(\widetilde{u}_i\widetilde{u}_i\right)_1^{0.5} / y_1 \tag{28}$$

$$l^{sgs} = \sqrt{k^{sgs}}\, y_1^2 / (0.53\nu) \tag{29}$$

where y_1 is the grid length scale of the first cells in the wall normal direction, and ν the kinematic viscosity. This set of condition, equations (28) and (29), has been tested for $y_1^+ < 5$ in this work. k^{sgs} is set to $(0.016u_\infty)^2$ and l^{sgs} is set to the local grid length scale Δ at far field. They are initialized with the same corresponding conditions also.

An efficient parallel version of the solver has been developed, based the Message-Passing Interface (MPI) library. For the parallelization and complex geometry applications, the computational domain is split into multi-blocks, and each block is decomposed into zones. Each zone is enclosed with up to three layers of ghost cells. The ghost cells store flow variables transferred from the neighboring zone as numerical boundary condition.

V. Numerical Results and Discussion

In the section, the realizable KES model has been applied to simulate the flows around a NACA-0015 airfoil/wing for 3D static stalls and 2D dynamic stalls. Numerical results are presented in comparison with experimental data (Piziali, 1994). In the experiment, the data for an oscillating NACA-0015 wing was obtained in a 7×10 foot wind tunnel at the NASA Ames Research center. The flow conditions of the experiment are as follows: free stream Mach number $M_\infty = 0.29$, Reynolds number $\mathbf{Re} = 1.95 \times 10^6$ based on the free stream velocity U_∞ and airfoil chord *C*.

In numerical simulations, Multiblock C-grid is used for the space discretization, as shown in Figure 1. The distance to the outer boundary is 8*C*. The normal distance from the first grid to the wall is $\Delta y_1 = 1 \times 10^{-5} C$, with $y_1^+ < 5$. In 2D simulations, the spanwise length is $z = 0.0012C$, the grid size is 541×97×2, which includes 391 points around the airfoil and 75 points in the wake, and 2 points in spanwise direction. In 3D simulation of wings, the spanwise length is $z = 0.08C$ with 21 points, and the other geometry and grid size are the same as those in 2D simulations. For the static airfoil/wing, angles of attack in the linear-lift and stall regime are simulated. For the oscillating airfoil, the instantaneous location of the airfoil surface is obtained from the pitching motion described in equation (30),

$$\alpha = \alpha_0 + \alpha_1 \sin(\omega t) \tag{30}$$

where $\omega = 2U_\infty k / C$ is the angle frequency of pitching, k the reduced frequency, α_0 the mean angle of attack in pitching, and α_1 the amplitude of the sinusoidal oscillation. Three pitching cases are simulated: attached flow with $\alpha_0 = 4^\circ$, $\alpha_1 = 4.2^\circ$ and $k = 0.1$; dynamic light stall with $\alpha_0 = 10.88^\circ$, $\alpha_1 = 4.22^\circ$ and $k = 0.1$; dynamic deep stall with $\alpha_0 = 13.03^\circ$, $\alpha_1 = 5.25^\circ$ and $k = 0.1$.

Validation of Realizability Constraints

The realizability constraint of equations 17(a-c) is checked in the simulation of 2D AoA 13° and 3D AoA 16°. In the case of 2D AoA 13° the realizability constraint is violated at less than four percent of grid points, while less than two percent in the case of 3D AoA 16°. This is attributed the coarse grid resolution in the region where strong shear exists. Numerical adjustment is necessary for C_ν with equation (25) and for l^{sgs} with equation (26).

Previous 2D cases of AoA13° and 16° (Fang and Menon, 2006) are re-computed with current realizable KES. There is not significant difference in the aerodynamics solution of pressure, lift, drag, and moment coefficient or the flow solution of velocity field, except the subgrid length scale. Figure 2 shows the realizable KES results for an instantaneous length scale around the NACA0015 airfoil at AoA=13°, with respect to the ratio of subgrid length scale to grid scale and pure subgrid length scale, respectively, in Figure 2(a) and 2(b). Similar results are

shown in Figure 3 for the simulation of AoA=16°. In both of the cases simulated, there is not stagnation-point singularity for the computed length scale as reported in the literature of k-ε model (Durbin, 1996). In Figures 2(a) and 3(a), the green region represents that the subgrid length scale is in the order of grid scale, and we say that the KES works as a LES model. The red region represents that the subgrid length scale is much greater than the grid scale, approaching the limit of integral length scale, and we say the KES works as a VLES model. In the very small region with blue color, the subgrid length scale is smaller than the grid scale, and the KES behaves as a DNS method. More details on the time-dependent behavior of KES will be presented in the following 3D simulations.

3D Static stall:

The KES solutions of the flow around a NACA0015 airfoil at different angles of attack were reported in previous work (Fang and Menon, 2006). The flow is stalled with massive separation and has a strong character of unsteadiness at AoA 16^o. It has been a big challenge to capture such unsteady physics with regular RANS models. KES is a VLES/LES model that is time accurate and should capture these unsteady features. In this work, 3D simulations around the NACA0015 wing at AoA 16° are performed to study the detailed behavior of the realizable KES model. The results are presented in this section. Physical time step of $\Delta t = 2.1\times10^{-6}$s is applied advance the integration with a dual-time stepping scheme. The flow develops and is sampled until time of 0.079sec.

Figure 4(a) shows the instantaneous streamlines around the 3D NACA0015 wing in the middle plane of spanwise direction at physical time 0.079sec, which represents a typical movement of separated vortices in static stall. Figure 4(b) represents the mean flow streamlines, which denotes the separation bubble in a time-averaged sense.

The averaged Reynolds stresses are shown in Figure 5. As shown in Figure 5(a), both the areas near the trailing edge and the suction region, from where vortex is shedding, have a high value of u_{rms}. v_{rms} is strong only in the wake region right after the trailing edge, as shown in Figure 5(b). Similar to u_{rms}, the antisymmetric stresses $\langle u'v' \rangle$ is more active in the suction region, as shown in Figure 5(c). From the contours of Reynolds stresses, it can be seen that turbulence dominates in both suction region and trailing edge. The averaged Reynolds stresses for 3D simulation are similar to those in 2D.

Figure 6 shows an instantaneous isosurface for the spanwise velocity around the 3D NACA0015 wing at about time 0.079sec. The spanwise velocity is always small in magnitude, since the flow is inherently 2D-predominant. The isosurface is at a level of 0.05m/s. Consistent with the instantaneous streamlines shown in Figure 4(a), the spanwise velocity develops from the leading edge and becomes a significant value in the region where the flow fully separates. The value decreases after a distance from the separation point, then increases in a region above the trailing edge. The variation is associated with the vortex shedding from leading and trailing edge of the wing. The spanwise distribution gives information to the 3D unsteady turbulence fluctuation, which is captured in this simulation. A typical pattern of spanwise vorticity distribution is presented in Figure 7 in the middle plane around the 3D NACA0015 wing. Again it can be seen that vortices are shed from the suction region and trailing edge.

Turbulence signals are probed and collected at ten points with locations shown in Figure 7. The Locations are selected to capture the vortex structure and to estimate the KES behavior in simulating the flow around the wing. Figure 8 shows a typical time evolution of the ratio of subgrid length scale to the grid scale at these ten grid points. The length scale ratios at points 1, 9 and 10, are shown in Figure 8(a). At these three points, the KES model behaves as LES since the time-averaged subgrid length scale is comparable to the grid scale. However, the KES model behaves as VLES in points 2-8, as shown in Figure 8(b), because the subgrid length scale is

usually much larger than the grid scale by one order in magnitude. The subgrid length scale has a strong character of unsteadiness for these ten points probed. As shown in Figure 8(a), the KES may behave as VLES sometime, although it works like LES most of time at points 1, 9 and 10. The KES may work as LES at point 3 at some time, although it works as VLES most of time. Therefore, the KES model switches between VLES and LES adaptively based on the its subgrid length scale, and the switching of the behavior is unsteady.

The frequency spectra analyses of the resolved velocity are performed and presented in Figure 9. Figure 9(a) shows the frequency spectra of E_{11} at point 1, where there exists an inertial range from about 500Hz to 2000Hz. The spectra in the inertial range matches the Kolmogorov-Obukhov spectrum (-5/3 law). Figure 9(b) represents the frequency spectra of E_{11} at point 10, where an inertial range exists from about 800Hz to 3000Hz. Similar inertial sub-range is captured at point 9. The captured inertial range represents the LES behavior of KES. However, the frequency spectrum of E_{11} at point 4 and 7, shown in Figure 9(c) and 9(d), respectively, does not show an inertial sub-range. That is, the KES model behaves as VLES at these points, which is consistent with Figure 8(b).

Airload analysis:

Previously KES was applied to predict the airloads around NACA0015 airfoil in 2D simulations (Fang and Menon, 2006), in a good agreement with experiment (Piziali, 1994) as shown in Figure 10. Similar work has been performed in ONERA (Gleize, *et al.* 2004) with various RANS models of Spalart-Allmaras, k-ω, k-ω with SST correction, k-ω with Kok modification, k-ω Kok + SST, *k-l*, k-ε, and multi-scale model. In the ONERA study, lift coefficient CL was overpredicted and drag coefficient CD was underpredicted after static stall, even with fine grids up to 3.5 million.

The airloads for the 3D AoA 16° are shown in Figure 10, compared with those in previous 2D simulations and experimental measurement. In Figure 10(a) the lift coefficients for 3D simulation is lower than that in 2D simulation, but still with the range of experimental measurement. The drag and moment coefficients for 3D simulation is a little higher than those in 2D simulation, with an good agreement with experimental measurement as shown in Figures 10(b) and 10(c), respectively.

2D Oscillatory Airfoil Flows:

The boundary conditions for flows over the pitching airfoil are similar to those used for the stationary airfoil. The tangential and normal velocities of the moving surface are equal to the surface grid velocities. The pressure is corrected by solving equation (27). For all the pitching cases, the reduced frequency is $k = 0.1$. The flow is initialized from a steady state solution before separation at the mean angle of attack, which is obtained through the scheme of local-time-stepping. For all the numerical solutions presented in this paper, the first cycle in transition is eliminated, and a physical time step of $\Delta t = 9.0 \times 10^{-6}\text{s}$ is employed to advance the solution.

Dynamic attached flow:

The NACA-0015 airfoil movies at a motion with the angle of attack $\alpha = 4^\circ + 4.2^\circ \sin(2kU_\infty t / C)$, resulting in an attached flow. This flow essentially serves to validate the accuracy of the flow solver and KES model in calculating unsteady attached flow. Due to the absence of flow separation, the airloads are found to be repeatable after the second period of airfoil oscillation. KES results of the unsteady airloads on the oscillatory airfoil are presented in Figure 11, compared with the experimental data. The lift coefficient C_L is under-predicted a little at the top of the upstroke, as shown in Figure 11(a). Figure 11(b) shows the drag coefficient C_D,

with a small under-prediction during the whole cycle. Figure 11(c) shows an over-prediction of the moment coefficient C_M during the whole cycle. C_M has a better agreement with experiment in the downstroke than in the upstroke. Generally the three airloads are in a good agreement with experimental measurement.

Dynamic light stall:

A case of dynamic light stall is simulated, where the NACA-0015 airfoil movies at a motion with $\alpha = 10.88^\circ + 4.22^\circ \mathbf{sin}(2kU_\infty t / C)$. In the experiment, a small region of flow begins to separate in the end of the upstroke. In this case, two cycles of flow are simulated after it finishes the transition from initial conditions. Figure 12 shows the airloads for each cycle, where cycle-to-cycle variations can be observed. As shown in Figure 12(a), the lift coefficient C_L compares well with experiment in the upstroke, but it is much more under-predicted in the downstroke. There is a small over-prediction of the drag coefficient C_D in all cycles, and C_D oscillates from the end of upstroke to the middle of downstroke, as shown in Figure 12(b). Figure 12(c) shows the momentum coefficient C_M. It can be seen that C_M agrees well with the experiment in the upstroke, while becomes higher in most of the downstroke. There are more obvious oscillations in C_M where C_D shows its oscillations. The character of oscillation is due to the flow separation and vortex shedding in the downstroke roughly between 15.1° and 9.6°. When visualizing the simulated flow field, it can be seen that the flow starts separation in a small region near the trailing edge in the end of the upstroke (about 15.1°), and persists more than half of the downstroke (about 9.6°). The phenomenon of vortex shedding is observed from the trailing edge when flow is separated. The flow becomes reattached after about AoA 9.6° in the downstroke and maintains attached until the end of the upstroke. Again in general, the KES results of airloads for this dynamic light stall case are in a good trend with experimental data.

Dynamic deep stall:

Another case of dynamic deep stall is simulated, where the NACA-0015 airfoil movies at a motion with $\alpha = 13.03^\circ + 5.25^\circ \mathbf{sin}(2kU_\infty t / C)$. The flow is fully separated in most of the airfoil oscillatory motion. Figure 13 shows the unsteady airload hysteresis for the deep stall. Seven flow cycles have been simulated. This number might not be enough to get a smoother average solution, since over twenty cycles of measurement were taken to get an averaged data in the experiment. In the upstroke, all the three airloads, lift coefficient C_L, drag coefficient C_D, and momentum coefficient C_M, have a very good agreement with experimental measurement. But there is an obvious overshoot of them in a short region of the downstroke roughly after the end of the upstroke, which is an interesting issue to be revisited in the future. Beyond this region, all the predicted airloads scatter around the value of measurement, and it would be expected that a few more cycles of solutions can be averaged to match the experimental data.

In the case of dynamic light stall, the vortex is shed from the trailing edge only. In this deep stall case, vortex is shed from the trailing edge as well as the leading edge. There is a complex unsteady interaction between the leading-edge vortex, also named "dynamic stall vortex", and the trailing-edge vortex. This interaction is dynamic stall phenomenon, which has been attracted intensively for tens of years in the community of aerodynamics. The overshoot problem observed in the airloads might be related to this interaction numerically. Figure 14 presents snapshots of the flow evolution in a typical cycle, where contours represent the magnitude of spanwise vorticity. Starting from the minimum angle of attack, the airfoil pitches in the upstroke. The upstroke acceleration has an effect on reducing the angle of attack, and increases the static stall limit, α_c, keeping the flow attached. As discussed in previous work (Fang and Menon, 2006), α_c is about 13° for NACA-0015 airfoil, where the flow starts mild

separation near the trailing edge. In the simulation of deep stall, the flow keeps attached in the upstroke until mild separation starts at about $\alpha = 15.24^\circ$, as shown in Figure 14. Roughly after $\alpha = 18.2^\circ$, the flow becomes fully separated in the upstroke. Near the end of the upstroke ($\alpha = 18.28^\circ$), there are obvious unsteady interactions among the leading-edge vortices and the trailing-edge vortices, and the leading-edge vortices dominate the vortex structure around the airfoil. When the airfoil changes its motion into downstroke, the vortex is shed with much stronger vorticity in the trailing edge due to the positive acceleration of airfoil. The vortex interactions become stronger, resulting in a clear vortex process of breakup-recombination-breakup. Only minor part of weakly recombined vortex structure moves into wake, while most of the broken eddies are dissipated in the region around the airfoil. This process dominates in the downstroke down to about $\alpha = 16.24^\circ$. Then the vortex shedding becomes weaker and major part of the vortex interaction moves into the wake. The flow separates only near the trailing edge after the downstroke of about $\alpha = 10.29^\circ$, and becomes attached again near the end of downstroke.

VI. Concluding Remarks/Future Plans

A two-equation VLES/LES model based on the *k-kl* approach is developed and demonstrated. A realizability constraint is used to limit the model coefficients. The subgrid length scale is found to be sensitive to the realizability constraints. A new model of compressible realizability constraints is proposed to improve the numerical oscillation in the flow region with strong shear. The realizable KES model has been applied to simulate static stall around a 3D NACA0015 wing and dynamic stall around a 2D NACA0015 airfoil. Vortex shedding and massive separation at high Reynolds number are clearly captured with satisfying accuracy. The detailed behavior of the realizable KES model on high AoA aerodynamics is studied.

In the future, a dynamic model for the coefficients of eddy viscosity and kinetic energy dissipation will be developed. Many issues still remain to be addressed. The current simulations were limited to airfoil flows. The KES model will be extended for more canonical flows such as isotropic turbulence and spatial shear layers. Finally a locally dynamic model for the estimation of model constants is being developed based on earlier work (Kim and Menon, 1999). This approach is needed to give general universality to the KES method.

Acknowledgement

This work is sponsored by DARPA under ARO Contract # W911NF-04-1-0419. Opinions, interpretations, conclusions, and recommendations are those of the authors and are not necessarily endorsed by the United States Government.

Reference:

1. Durbin, P.A., “On the k-3 stagnation point anomaly,” *Int, J. Heat and Flow Flow*, Vol. 17, pp. 89-90, 1996.
2. Fang, Y. and Menon, S., "*A New Two-Equation Subgrid Model for Large-Eddy Simulation of High Renolds Number Flows*," AIAA Paper 2006-0116, 44th AIAA Aerospace Science Meeting and Exhibit, Reno, NV, 2006.
3. Girimaji, S. S. and Abdol-Hamid, K. S., “Partially-Averaged Navier-Stokes Model for Turbulence: Implementation and Validation,” AIAA Paper 2005-0502, 43rd AIAA Aerospace Science Meeting and Exhibit, Reno, NV, 2005.
4. Jameson, A., “Time Dependent Calculations Using Multigrid, with Applications to Unsteady Flows Past Airfoils and Wings,” AIAA Paper 91-1596, 1991.

5. Jameson, A., "Transonic Flow Calculations," in *Numerical Methods in Fluid Dynamics*, edited by F. Brezzi, Lecture Notes in Mathematics, Vol. 1127, pp. 156-242, Springer-Verlag, 1985.
6. Jameson, A., Schmidt, W. and Turkel, E., "Numerical Solution of the Euler Equations by Finite Volume Methods using Runge-Kutta Time-Stepping Schemes," AIAA Paper 81-1259, 1981.
7. Kim, W.W. and Menon, S., "A New Incompressible Solver for Large-Eddy Simulation," International Journal of Numerical Fluid Mechanics, Vol. 31, pp. 983-1017, 1999.
8. Lakshmipathy, S. and Girimaji, S. S., "Partially-Averaged Navier-Stokes Method for Turbulent Flow: k-ω model implementation," AIAA Paper 2006-0119, 44th AIAA Aerospace Science Meeting and Exhibit, Reno, NV, 2006.
9. Mellen, C.P., Fröhlich, J. and Rodi, W., "Lessons from LESFOIL Project on Large-Eddy Simulation of Flow around an Airfoil," *AIAA Journal.* Vol. 41, No. 4, 2003.
10. Menon, S. and Kim, W.W., "High Reynolds Number Flow Simulations Using the Localized Dynamic Subgrid Model," AIAA Paper 96-0425, 1996.
11. Nelson, C. and Menon, S., "Unsteady Simulations of Compressible Spatial Mixing Layers," AIAA Paper 1998-0786, 36th Aerospace Sciences Meeting and Exhibit, Reno, NV, 1998.
12. Piomelli, U. and Balaras, E., "Wall-Layer Models for Large-Eddy Simulations," *Annu. Rev. Fluid. Mech.* Vol. 34, pp. 349-74, 2002.
13. Piomelli, U. and Chasnov, J.R., "Large-Eddy Simulations: Theory and Applications," in Henningson, D., Hallbäck, M., Alfredsson, H. and Johansson, A., *Transition and Turbulence Modeling*, pp. 269-336, Doredrecht, Kluwer Academic Publishers, 1996.
14. Piziali, R.A., "2-D and 3-D Oscillating Wing Aerodynamics for a Range of Angle of Attack Including Stall," NASA-TM-4632, September 1994.
15. Sankar, L, Zibi-Bailly, J., Le Baeur, J.C., Blaise, D., Rouzand O. and Rhee, M., "A Comparative Study of Three Methodologies for Modeling Dynamic Stall," 28th European Rotorcraft Forum, Bristol, 2002.
16. Schumann, U., "Realizability of Reynolds-Stress Turbulence Models," *Phys. of Fluids*, Vol. 20. No. 5, pp. 721, 1977.
17. Smagorinsky, J., "General Circulation Experiments with the Primitive Equations, I. The Basic Experiment," Monthly Weather Review, Vol. 91, pp. 99, 1963.
18. Spalart, P.R., Jou, W-H., Strelets, M. and Allmaras, S.R., "Comments on the Feasibility of LES for Wings, and on the Hybrid RANS/LES Approach," in *Advances in DNS/LES*, 1st AFOSR Int. Conf. on DNS/LES, Greyden Press, Columbus Oh, Aug. 4-8, 1997.
19. Squires, K.D., "Detached-Eddy Simulation: Current Status and Perspective," in *Proceedings of Direct and Large-Eddy Simulation V*, 2004.
20. Vreman, B., Geurts, B. and Kuerten, H., "Realizability Conditions for the Turbulent Stress Tensor in Large Eddy Simulation," *J. Fluid Mech.*, Vol. 278, pp. 351, 1994.
21. Chakravarthy, V. and Menon, S., "Large-Eddy Simulations of Turbulent Premixed Flames in the Flamelet Regime," *Comb. Sci. and Tech.*, Vol. 162, pp. 175, 2001.

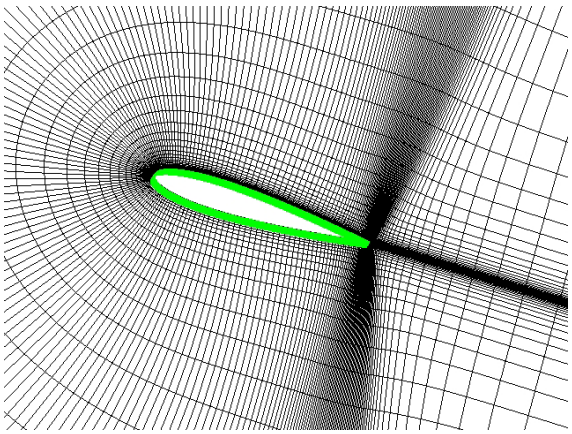

Figure 1. Multiblock C-grid around NACA-0015 wing, every 2nd point is shown in each direction.

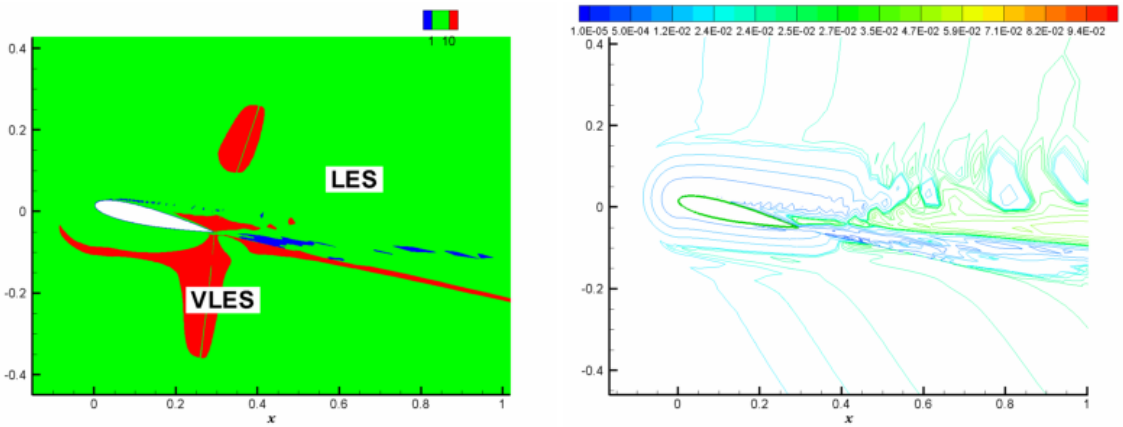

2(a) l^{sgs}/Δ 2(b) l^{sgs}

Figure 2. Contours of instantaneous length scale around NACA0015 airfoil at AoA=13°, by realizable KES. (a): l^{sgs}/Δ; (b): l^{sgs}.

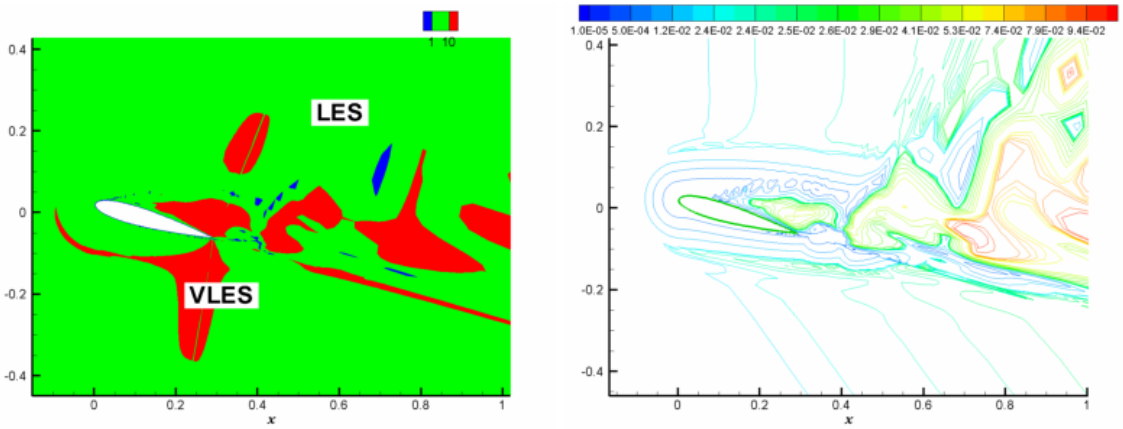

3(a) l^{sgs}/Δ 3(b) l^{sgs}

Figure 3. Contours of instantaneous length scale around NACA0015 airfoil at AoA=16°, by realizable KES. (a): l^{sgs}/Δ; (b): l^{sgs}.

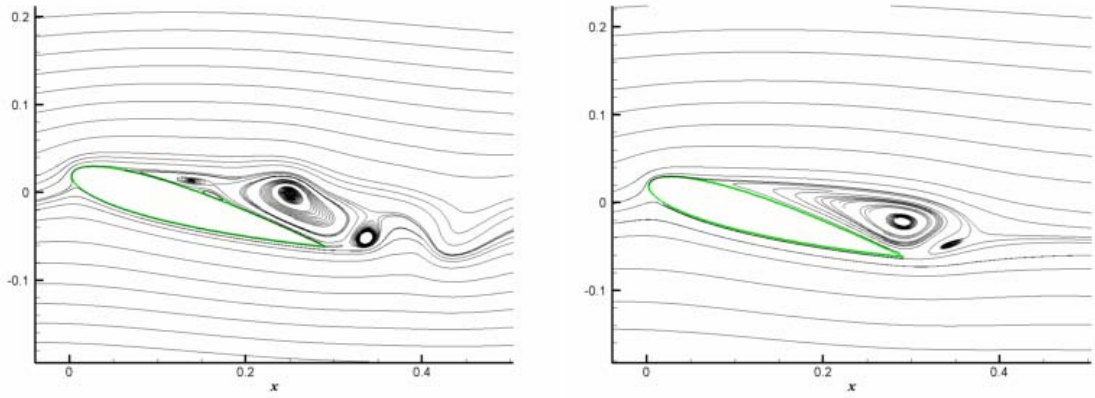

4(a) Instantaneous 4(b) Time-averaged

Figure 4. Flow streamlines around 3D NACA0015 wing, at AoA = 16°, by realizable KES. (a): instantaneous; (b): time-averaged.

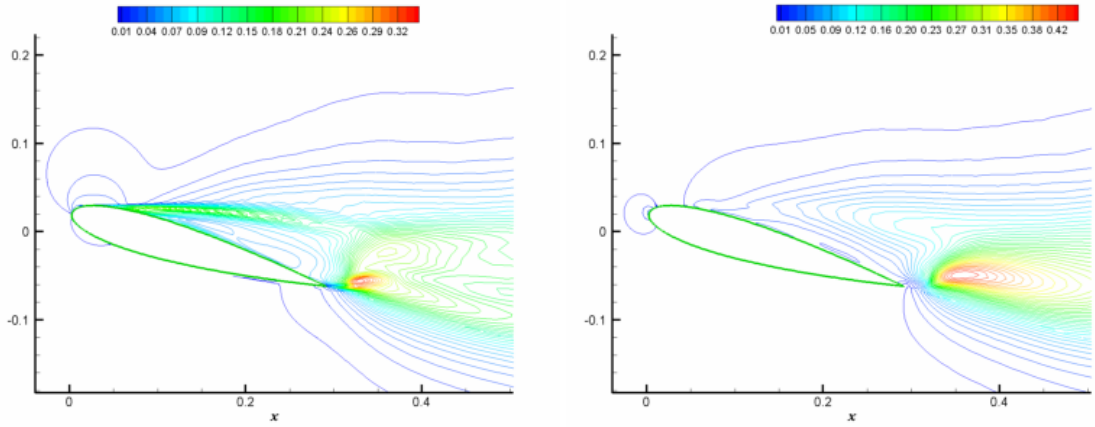

5(a) u_{rms}/u_∞. 5(b) v_{rms}/u_∞.

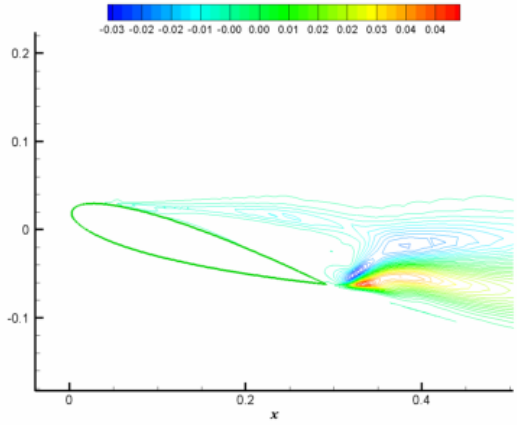

5(c) $\langle u'v' \rangle / u_\infty^2$.

Figure 5. Contours of time-averaged Reynolds stress around a 3D NACA0015 wing at AoA=16°.
(a): u_{rms}/u_∞; (b): v_{rms}/u_∞; (c): $\langle u'v' \rangle / u_\infty^2$.

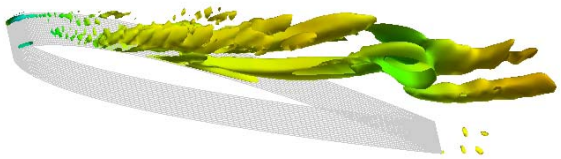

Figure 6. Instantaneous isosurface for spanwise velocity of 0.05.

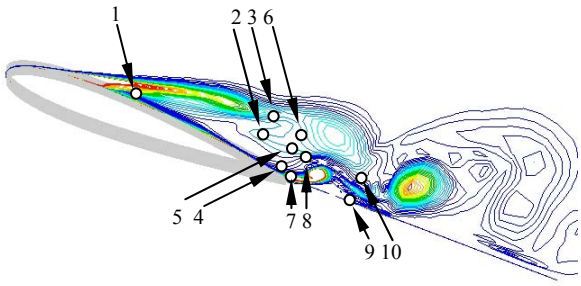

Figure 7. Contours of instantaneous spanwise vorticity and probe points for turbulence signal in the middle z-plane.

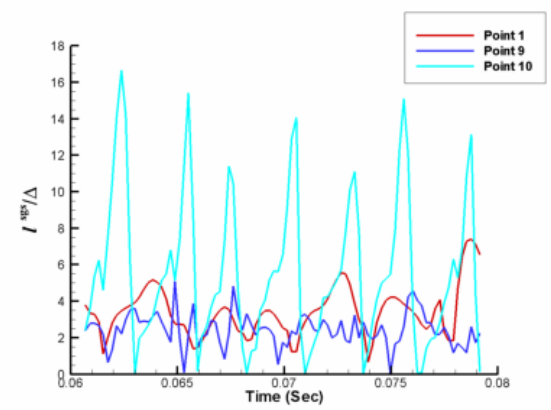

8(a) Point 1, 9 and 10.

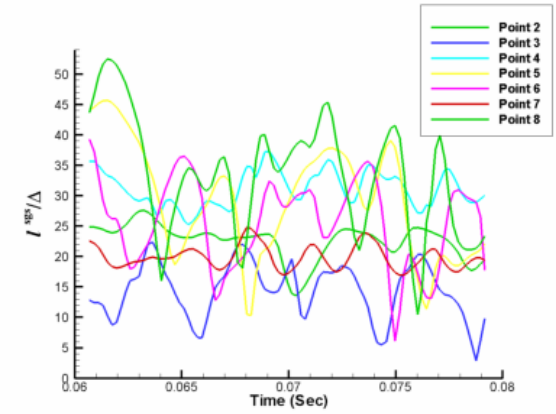

8(b) Point 2-8.

Figure 8. Typical evolution of the ratio of subgrid length scale to grid scale at probed points. (a): point 1, 9 and 10; (b) point 2-8.

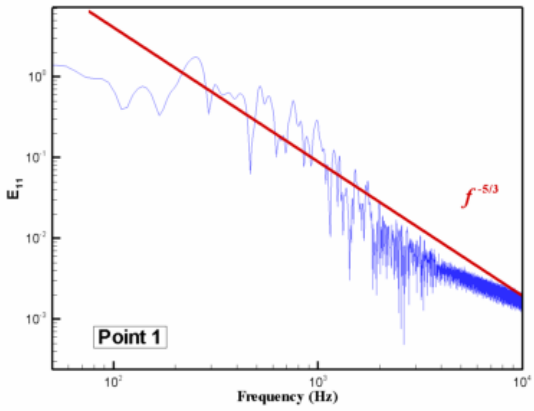

9(a)

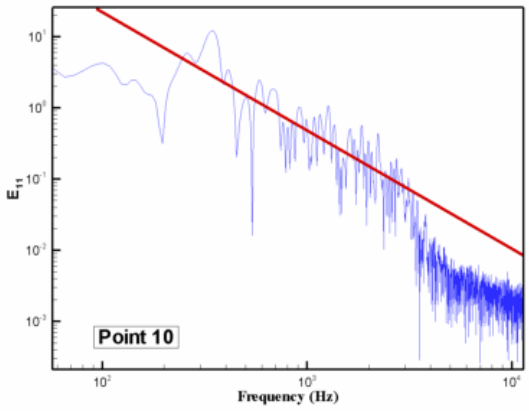

9(b)

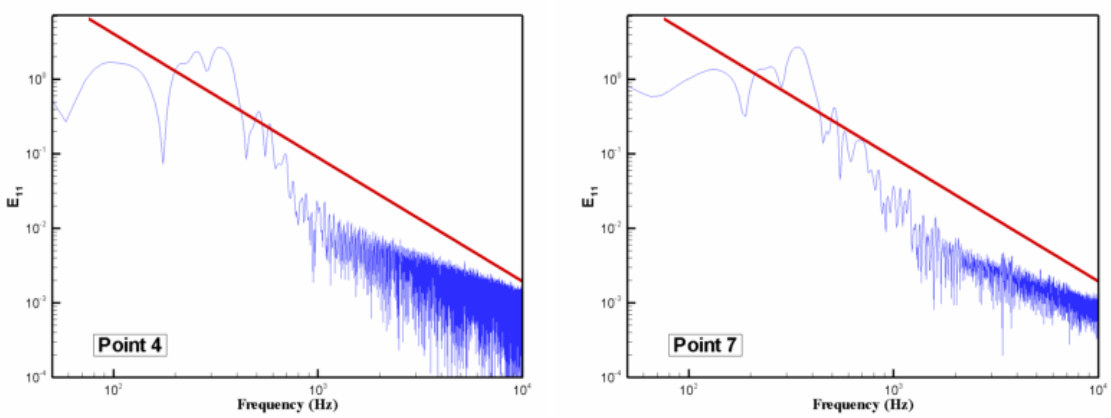

9(c) 9(d)

Figure 9. Frequency spectrum of the resolved velocity u at different points around 3D NACA0015 wing, AoA=16° .

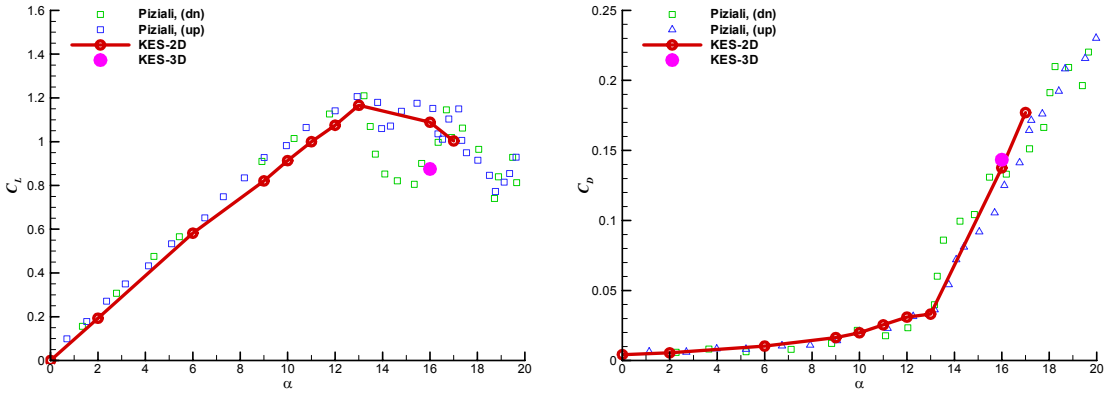

10(a) Lift coefficient. 10(b) Drag coefficient.

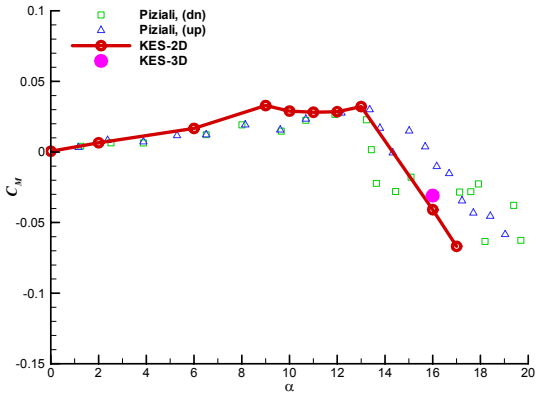

10(c) Moment coefficient.

Figure 10. Comparison of the airloads around NACA-0015 airfoil/wing between KES results and experimental measurement. (a): Lift coefficient; (b): Drag coefficient; (c): Moment coefficient.

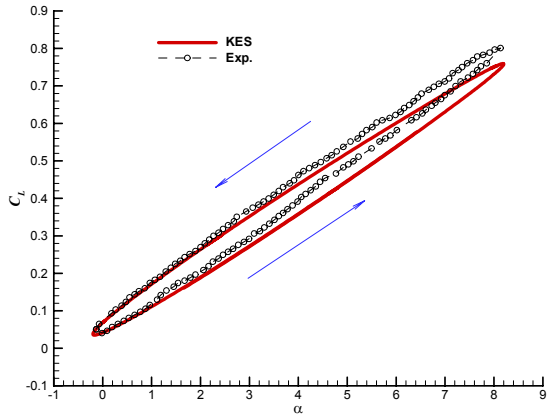

11(a) Lift coefficient.

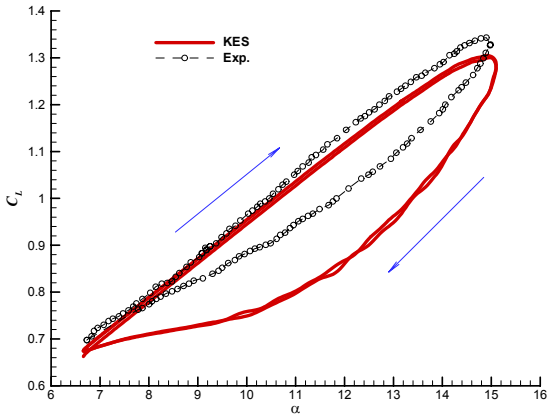

12(a) Lift coefficient.

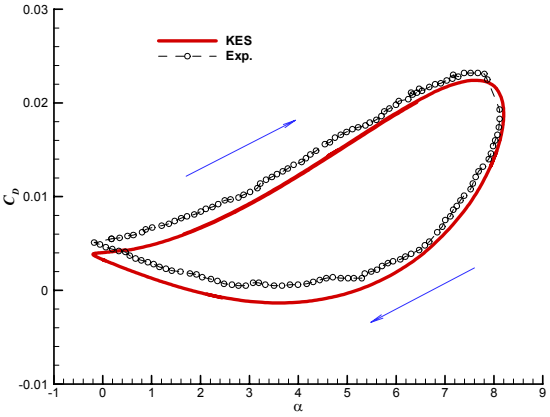

11(b) Drag coefficient.

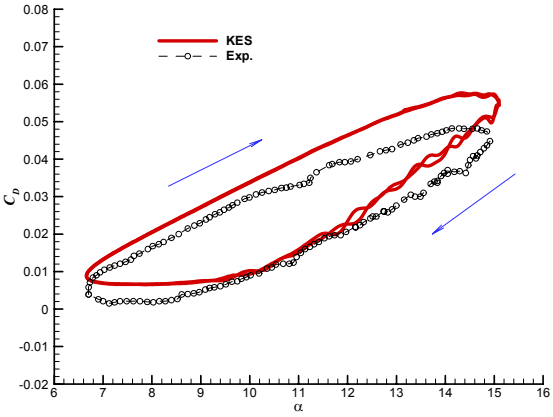

12(b) Drag coefficient.

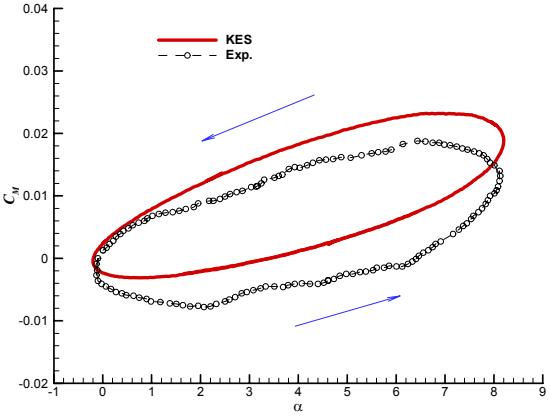

11(c) Momentum coefficient.

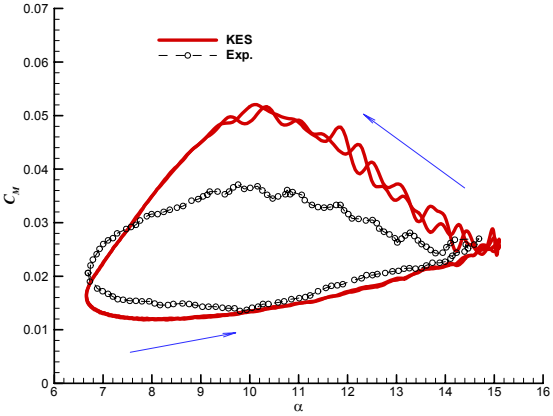

12(c) Momentum coefficient.

Figure 11. Airloads hysteresis for the dynamic attached flow around NACA0015 airfoil, with $\alpha = 4^\circ + 4.2^\circ \sin(2kU_\infty t / C)$, $k = 0.1$, $M_\infty = 0.29$, $\mathbf{Re} = 1.95 \times 10^6$. (a): Lift coefficient; (b): Drag coefficient; (c): Moment coefficient.

Figure 12. Airloads hysteresis for the dynamic light stall around NACA0015 airfoil, with $\alpha = 10.88^\circ + 4.22^\circ \sin(2kU_\infty t / C)$, $k = 0.1$, $M_\infty = 0.29$, $\mathbf{Re} = 1.95 \times 10^6$. (a): Lift coefficient; (b): Drag coefficient; (c): Moment coefficient.

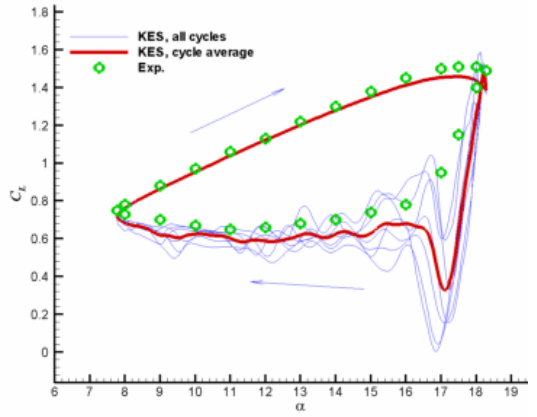

13(a) Lift coefficient.

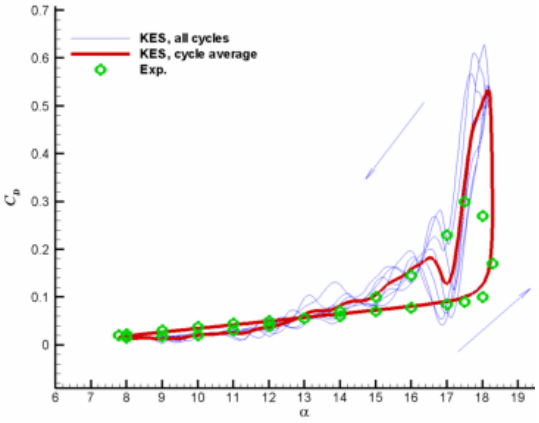

13(b) Drag coefficient.

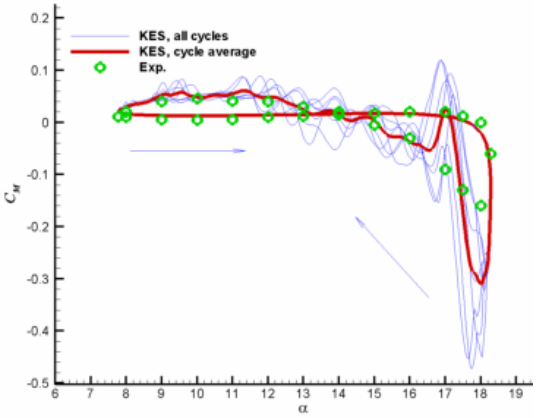

13(c) Momentum coefficient.

Figure 13. Airloads hysteresis for the dynamic deep stall around NACA0015 airfoil, with $\alpha = 13.03^\circ + 5.25^\circ \sin(2kU_\infty t/C)$, $k = 0.1$, $M_\infty = 0.29$, $\mathbf{Re} = 1.95 \times 10^6$. (a): Lift coefficient; (b): Drag coefficient; (c): Moment coefficient.

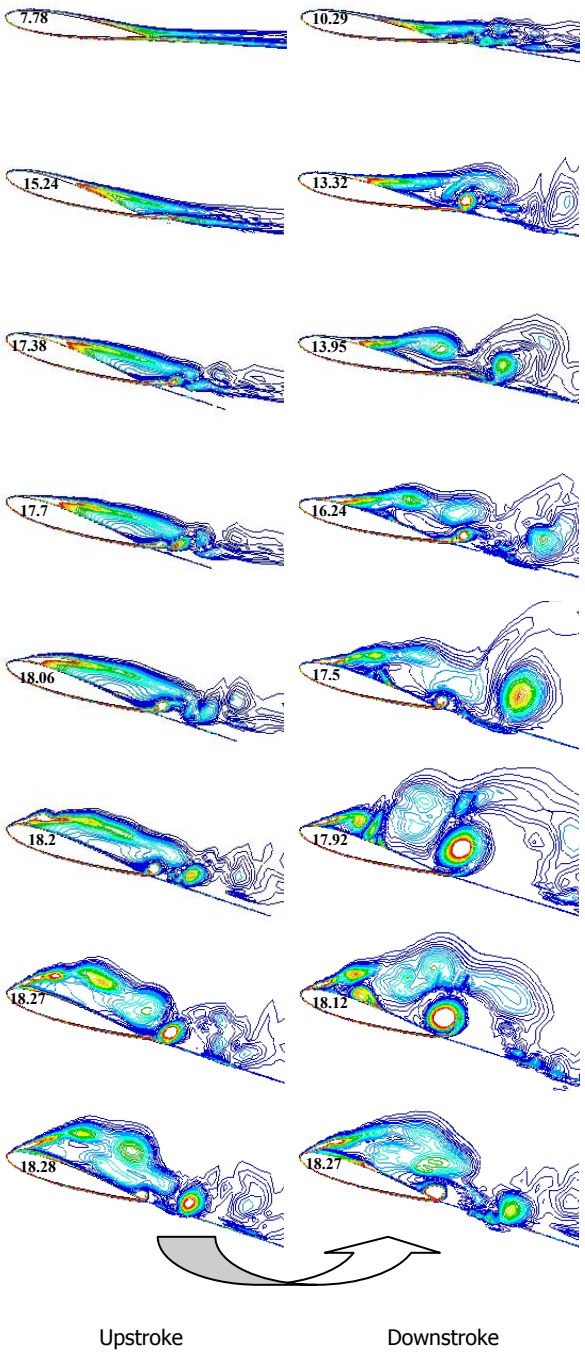

Figure 14. Instantaneous contours of vorticity magnitude for the dynamic deep stall around NACA0015 airfoil, with $\alpha = 13.03^\circ + 5.25^\circ \sin(2kU_\infty t/C)$, $k = 0.1$, $M_\infty = 0.29$, $\mathbf{Re} = 1.95 \times 10^6$.